CARDIFF UNIVERSITY
PRIFYSGOL CAERDYDD

ORCA – Online Research @ Cardiff

This is an Open Access document downloaded from ORCA, Cardiff University's institutional repository:https://orca.cardiff.ac.uk/id/eprint/107640/

This is the author's version of a work that was submitted to / accepted for publication.

Citation for final published version:

Tang, Fengzai, Lee, Kean B., Guiney, Ivor, Frentrup, Martin, Barnard, Jonathan S., Divitini, Giorgio, Zaidi, Zaffar H., Martin, Tomas L., Bagot, Paul A., Moody, Michael P., Humphreys, Colin J., Houston, Peter A., Oliver, Rachel A. and Wallis, David 2018. Nanoscale structural and chemical analysis of F-implanted enhancement-mode InAlN/GaN heterostructure field effect transistors. Journal of Applied Physics 123 (2) , 024902. 10.1063/1.5006255

Publishers page: http://dx.doi.org/10.1063/1.5006255

Please note:
Changes made as a result of publishing processes such as copy-editing, formatting and page numbers may not be reflected in this version. For the definitive version of this publication, please refer to the published source. You are advised to consult the publisher's version if you wish to cite this paper.

This version is being made available in accordance with publisher policies. See http://orca.cf.ac.uk/policies.html for usage policies. Copyright and moral rights for publications made available in ORCA are retained by the copyright holders.

Nanoscale structural and chemical analysis of F-implanted enhancement-mode InAlN/GaN heterostructure field effect transistors

Fengzai Tang,[1] Kean B. Lee,[2] Ivor Guiney,[1] Martin Frentrup,[1] Jonathan S. Barnard,[1] Giorgio Divitini,[1] Zaffar H. Zaidi,[2] Tomas L. Martin,[3] Paul A. Bagot,[3] Michael P. Moody,[3] Colin J. Humphreys,[1] Peter A. Houston,[2] Rachel A. Oliver,[1, a)] and David J. Wallis,[1, 4]

[1]*Department of Materials Science and Metallurgy, University of Cambridge, 27 Charles Babbage Road, Cambridge, CB3 0FS, UK.*

[2]*Department of Electronic and Electrical Engineering, University of Sheffield, Mappin Street, Sheffield, S1 3JD, UK*

[3]*Departments of Materials, University of Oxford, Parks Road, Oxford, OX1 3PH, UK*

[4]*Center for High Frequency Engineering, University of Cardiff, Cardiff, CF24 3AA.*

We investigate the impact of a fluorine plasma treatment used to obtain enhancement-mode operation on the structure and chemistry at the nanometer and atomic scales of an InAlN/GaN field effect transistor. The fluorine plasma treatment is successful in that enhancement mode operation is achieved with a + 2.8 V threshold voltage. However, the InAlN barrier layers are observed to have been damaged by the fluorine treatment with their thickness being reduced by up to 50%. The treatment also led to oxygen incorporation within the InAlN barrier layers. Furthermore, even in the as-grown structure, Ga was unintentionally incorporated during the growth of the InAlN barrier. The impact of both the reduced barrier thickness and the incorporated Ga within the barrier on the transistor properties have been evaluated theoretically and compared to the experimentally determined two dimensional electron gas density and threshold voltage of the transistor. For devices without fluorine treatment, the two dimensional electron gas density is better predicted if the quaternary nature of the barrier is taken into account. For the fluorine treated device not only the changes to the barrier layer thickness and composition but also the fluorine doping needs to be considered to predict device performance. These studies reveal the factors influencing the performance of these specific transistor structures and highlight the strengths of the applied nanoscale characterisation techniques in revealing information relevant to device performance.

I. INTRODUCTION

Group III-nitride semiconductor materials, AlN, GaN, InN and their alloys, have a wide range of bandgaps from 0.7 eV (α-InN) to 6.2 eV (α-AlN).[1] Thus, this material system has not only formed the basis of the new-generation of light emitting diodes (LEDs)[2], but has also found increasing application in high electron mobility transistors (HEMTs) with potential applications at high powers, in the radio frequency regime and in robust solid state chemical sensors.[3-5]

GaN-based HEMTs with AlGaN barrier layers have been demonstrated with high breakdown voltages, high output power densities and terahertz emission and detection[6,7]. However, due to the large mismatch between the natural lattice parameters of AlGaN and GaN, the risk of strain relaxation in the AlGaN barrier on top of the GaN channel raises concerns about the reliability of these devices.[8] Also the mismatch is exacerbated as the Al-fraction is increased to achieve higher carrier densities and thus limits the potential of this technology for high output power density devices.[9] In order to overcome this limitation, growth of structures based on lattice

a) Author to whom correspondence should be addressed: rao28@cam.ac.uk.

^{2}-matched $In_xAl_{1-x}N$/GaN (x ~ 0.17) structures has been developed[10]. These InAlN devices provide more freedom in barrier thickness design, since InAlN also has a larger spontaneous polarisation field.[11] This gives rise to a higher charge density in the 2DEG (two dimensional electron gas) and allows reduced barrier thickness which is advantageous for shorter gate length devices. This would also favour high speed operation and mitigate short-channel effects.[12,13] Gonschorek *et al.* has reported a 2DEG density up to 1.7×10^{13} cm^{-2} on a lattice matched InAlN/GaN device with a 6 nm barrier thickness.[14]

In power control applications and digital circuits[15], depletion-mode (D-mode) HEMT devices are not optimal due to the fact that when the gate is unbiased a short circuit is present between source and drain which could cause safety issues in the event of a circuit failure. Hence, there is a strong motivation to develop enhancement-mode (E-mode) devices that enable normally-off function. A number of approaches have been developed to obtain E-mode operation: for instance, a p-type GaN layer deposited on top of the AlGaN barrier under the gate[16,17]; a recessed gate in which the barrier is thinned under the gate to deplete the 2DEG[18-20]; and an implanted gate where atoms with large electronegativity, such as fluorine (F), are incorporated into the barrier, again to deplete the 2DEG.[11-13,15,21-25]

Each technique has its own associated advantages and drawbacks. In the recessed-gate thinning approach, the barrier depletes the 2DEG under the gate and thus shifts the threshold voltage in the positive direction, but at the same time it also reduces the mobility of carriers under the gate, resulting in a low drain current.[11,16] The F-implantation approach has been increasingly employed in the fabrication of E-mode devices since it was first reported for AlGaN-based HEMTs by Cai *et al.*[24] in 2005 and for InAlN-based devices by Medjdoub *et al.*[25] in 2008. Compared to the recessed-gate method, this technique may improve breakdown voltage and/or mitigate gate tunnelling through control of the gate barrier thickness.[25]

In terms of E-mode operation of GaN-based HEMTs, a further improvement may be obtained by introducing an insulating layer, such as SiN_x or Al_2O_3, between the gate contact and the nitride semiconductor surface. Such devices are known as Metal-Insulator-Semiconductor Heterostructure Field-Effect Transistors (MISHFETs). This type of structure has been shown to provide advantages in the realization of a large positive threshold voltage, suppression of thermionic emission and mitigation of high-temperature tunnelling.[26,27] For example, an E-mode InAlN-based MISHFET fabricated utilising F-treatment of the gate barriers and a SiN_x insulating layer has demonstrated a + 3 V threshold voltage.[11,21] However, a variety of F-treatment conditions has been reported. For example, RF powers of 75 W - 600 W were used in the fabrication of AlGaN-based devices[11,15,24] and of 75 W- 200 W for producing InAlN-based devices[11,21-23,28]. Among these reports, a marginal reduction of barrier thickness as a result of plasma treatments (RF 150 W) was noticed by Cai *et al.* in 2006 on an AlGaN-based structure based on Atomic Force Microscopy (AFM) measurements.[15] Similarly, Hu *et al.* in 2014 also used AFM to identify the etching of InAlN layers caused by CF_4-based plasma treatment, where a larger etching rate was found at a higher RF power (150 W).[22] Despite its wide applications as a critical technique in fabricating E-mode devices, there is a lack of nanoscale understanding of material and device structures following the F-treatment process, although such analysis could provide information to drive improvements in the device fabrication process and the optimization of device performance.

Building on recent advancements in nanostructural analysis, in this work we have applied aberration-corrected Transmission Electron Microscopy (TEM)[29,30] and Atom Probe Tomography (APT)[30-33] to the characterization of InAlN-based E-mode MISHFET structures following F-plasma treatment. In order to precisely correlate the fabrication processes (both wafer and device) with the nanoscale structure and device performance, a dual beam Focused Ion Beam - Scanning Electron Microscopy (FIB-SEM) was used to prepare specimens from both

unprocessed HEMT structures and fabricated devices. The correlative study has provided structural and chemical information at the nanometer and atomic scales about the devices.

II. EXPERIMENTAL PROCEDURE

The HEMT structures were grown on 150mm diameter Si (111) wafers using Metal-Organic Vapour Phase Epitaxy (MOVPE). The layer structure consisted of a 240 nm AlN nucleation layer, followed by an AlGaN transition layer (~800 nm thick.) with a graded Al content, a 2.2 µm thick C-doped GaN buffer layer and a 250 nm undoped GaN channel. The barrier layer consisted of a 1 nm AlN layer and a nominally lattice matched 12 nm $In_xAl_{1-x}N$ (x = 0.17) layer followed by a 2 nm GaN cap, all grown at 775 °C at a pressure of 70 mbar using nitrogen as the carrier gas. Trimethyl-aluminium, trimethyl-indium, trimethyl-gallium and ammonia were used as precursors. Some more details of the growth process may be found in reference [21].

MISHFET devices were fabricated on the above structures using a standard procedure, as detailed in reference [21]. Mesa isolation was first carried out using inductively coupled Cl_2-based plasma etching. The source and drain ohmic contacts (Ti/Al/Ni/Au: 20/120/20/45 nm) were thermally evaporated and then annealed at 830°C under a nitrogen ambient. A 100 nm SiN_x passivation layer was deposited by Plasma-Enhanced Chemical Vapor Deposition (PECVD), into which a 1.5 µm gate window was opened for F-implantation using a reactive ion etching process. In order to obtain E-mode operation, F-implantation was carried out in an inductively coupled plasma chamber with a 40 sccm (standard cubic centimeter per minute) CHF_3 gas flow and an RF power of 100 W, applied for 15 mins. Thereafter, a 20 nm Al_2O_3 gate insulating dielectric layer was deposited using Atomic Layer Deposition (ALD) using an Oxford Instruments: Plasma OpAL reactor. Following standard calibration procedures, cycles of trimethyl aluminium and H_2O with an intervening Ar purge were used to fabricate Al_2O_3 oxide layers. The temperature of substrate was maintained at 200°C during deposition. (See reference [34] for details). The structure was then annealed at 500 °C for 5 minutes under a nitrogen gas environment in a rapid thermal annealing chamber. The chosen parameters are based on the previous study for obtaining an optimum positive threshold.[11] Finally, a Ni/Au (20/300 nm) gate metal layer was deposited prior to the fabrication of probe pad metals. The fabricated MISHFET had nominal dimensions of a 1.5 µm gate length, a 100 µm gate width, a 3.5 µm gate-source separation and a 10 µm gate-drain spacing. Figure 1a presents a schematic illustration of cross-section of the designed devices. In addition to the device structures, wafers were also prepared where the epilayers were blanket exposed to the F-implant process under identical conditions but no other fabrication was carried out.

The cross-sectional TEM specimens were prepared from as-grown and F-implanted epilayers and fabricated devices using a dual beam FIB-SEM FEI Helios NanoLab™ (Hillsboro, Oregon, USA). To minimize surface damage induced by FIB processing, a low FIB acceleration voltage was utilized at the final stage, similar to that in reference [30]. Samples were prepared from device structures at the gate region. A FEI Titan^3 TEM (80-300 kV) with a probe forming corrector for spherical aberration was used for high resolution High-Angle Annular Dark Field (HAADF) imaging. An analytical FEI TEM (Tecnai Osiris) fitted with an extreme Schottky Gun (FEI's XFEG) was used for chemical mapping operated in STEM mode at 200 kV. This instrument has an Energy Dispersive X-ray Spectrometer (EDS) composed of four large area detectors, designed for high quality chemical mapping. EDS mapping data were processed using an open source program, Hyperspy,[35] implementing a PCA (Principal Component Analysis[36]) algorithm that was employed for noise reduction.[35]

APT specimens were prepared from as-grown and F-implanted epilayers using dual beam FIB/SEM employing the procedures described in references [37,38] involving low FIB acceleration voltage milling to minimise FIB-induced damage. APT was conducted in pulsed-laser mode using Cameca instruments: LEAP 3000X HR and

LEAP 5000XR systems, both fitted with a reflectron for high resolution mass spectrometry analysis. F-treated epilayers were analyzed using the LEAP 3000X HR at 109 pJ laser energy per pulse, and as-grown structures were examined using the LEAP 5000XR at 0.050 pJ. The base temperature of sample stage was maintained at 30 K, and a constant detection rate of 0.005 atoms per laser pulse, as well as a constant laser pulse frequency of 200 kHz, was used for all APT analysis. APT reconstruction was done using the CAMECA IVAS^{TM} software package based on the thickness of the HEMT epilayers measured by TEM and/or the geometry of the APT specimen tip examined by FIB/SEM. Since the fluorine level was below the APT detection limit, Secondary Ion Mass Spectrometry (SIMS) depth profiling was used to determine the fluorine levels at Evans Analytical Group Laboratories (EAG, Inc.), again examining the epilayers which were F-implanted and annealed using the same settings as those used for device fabrication.

III. RESULTS AND DISCUSSION

A. Analysis of processed device structures

The surface view of a fabricated MISHFET is shown in Figure 1b. Figure 1c presents gate transfer characteristics of three fabricated devices, with the data from the device presented in Figure 1b marked with a circle. Although divergence in the measured drain current can be seen in the high voltage region amongst these three devices, a current larger than 10 mA/mm can be generally obtained at 7 V. Defining the threshold voltage (V_{th}) as the intercept on the gate bias axis found by linearly extrapolating the I-V curve at the point of peak transconductance, an average value of 2.8 ± 0.2 V can be found. Room temperature Hall measurement on another as-grown wafer with the same nominal HEMT structures revealed an electron mobility of 1700 $cm^2 V^{-1} s^{-1}$ and a 2DEG density of $1.3 \pm 0.1 \times 10^{13}$ cm^{-2}.

The device (Figure 1b) was analyzed at the position indicated by the yellow dotted line where a TEM lamella was extracted using dual beam FIB-based in situ lift-out approach. Figure 1d shows a STEM overview of the gate region, in which a gate window in the SiN_x passivation layer, about 1.4 µm wide, has been opened by reactive ion etching. High resolution STEM-BF imaging of this F-treated region (Figure 1e) reveals the atomic structure of the InAlN/AlN/GaN layers. The most striking feature observed is the low InAlN layer thickness. Furthermore, the GaN cap layer cannot be observed. The measured thickness of the InAlN/AlN layers was 5.7 ± 0.5 nm, approximately 50% of the design value. The thickness of the InAlN layer also appears to be uneven. Whilst the crystalline atomic planes are resolved across most layers, some areas in the vicinity of upper InAlN layer/ Al_2O_3 interfaces appear less crystalline in nature. One such region is indicated by an arrow. The thinning of the InAlN, the variations in thickness observed and the presence of regions with poor crystallinity are likely to be a consequence of the F-implantation process. The amorphous nature of the dielectric (20.8 ± 0.6 nm thick) is confirmed by high resolution imaging and nanodiffraction.

In Figure 1f, an overview of the edge of the gate window is shown, which confirms that in the F-treated region, there is significant thinning of the InAlN layer. The image also reveals a slight thinning of the gate dielectric on the side walls of the gate window which has a side angle θ of 67 ± 3° with respect to the wafer surface. The corner of the gate recess also shows a rounded profile which is important for controlling the electric fields in this region of the device. It is also seen that the Al_2O_3 dielectric shows good coverage of the recess topology as expected for an ALD deposition process. A further examination (Figure 1g) at a higher magnification illustrates the local variation in the thickness of the crystalline InAlN barrier layer at the edge of the gate recess. The thickness of the crystalline InAlN varies over a distance of ~ 20 nm. This tapering at the edge of the gate recess may effectively avoid the generation of high-field spikes which could promote impact ionisation in the GaN channel, resulting in the off-state breakdown.[39] The identified geometric configuration of gate edge may be used

in the realistic modelling of electric field distributions. Interestingly, a threading dislocation in the region of gate edge is also observed in this image as a grey line extended from the GaN buffer layer to the surface, as indicated by the arrow in Figures 1f (and also seen in Figure 1g). In Figure 1g some electron beam induced damage is evident in the dielectric layers (and is labelled as such), although the analysis was carried out at 80 kV in STEM.

Elemental mapping of the gate region is depicted in Figure 2. In order to minimize beam damage in the specimen, a relatively fast mapping setting was employed, so that the analysis is only semi-quantitative. Figure 2a is a STEM-BF image, where the rectangular region indicates the analyzed area (15.4 × 30.8 nm). Elemental O, Al, In, Ga and N distributions are presented in Figures 2b, c, d, e and f respectively. A compositional profile taken along a line of width 15 nm at the position indicated by the dotted line in (a) is shown in Figure 2g. According to the measured thickness of InAlN/GaN layers, the interface of InAlN/Al_2O_3 should be at around 5.7 nm, as indicated by the dotted vertical lines in the figure.

Starting from around 40 at. %, the Ga profile gradually decreases to 23 at. % at the 2 nm position and reaches the background level at the 8 nm position. In contrast, the oxygen level shows large variations across the examined region rising to about 6 at. % at the 2.5 nm position before rising to >50% at the InAlN/AlOx interface. On the other hand, the In profile shows relatively small variations within the range of 6 - 9 at.% for the first 4 nms, before tailing off to the background level at ~ 7 nm. A sharp increase in the Al profile can found from about 10 at. % at the initial point to 26 at. % within the 3 nm range. Due to both the interaction volume between the electron beam and the sample, and projection effects, some smearing of the composition profiles is expected at layer interfaces. For example, although the TEM lamella was well aligned with *m*-direction <1-100>, a mis-orientation of 0.3 degrees which is in general within the alignment errors could lead to ~ 0.5 nm overlap at the interfaces for a 100 nm thick lamella. Thus, at least some of the sharp rises in the Ga and O profiles at the GaN/InAlN and InAlN/AlOx interfaces respectively are due to resolution effects. However, there is clear evidence for significant O and Ga within the nominally InAlN layer. It is speculated that the oxygen is due to trace oxygen present in the atmosphere during the F-implantation process which leads to its incorporation in the films.

Since the electron-beam induced damage to the samples may have hindered the accurate STEM-EDS compositional characterisation, APT analysis of barrier layers extracted from devices was attempted. However, it was found that the APT samples tended to fracture in the course of the evaporation transition from the Ni layer to the AlO_x dielectric and/or to the barrier layers. This might be due to the strong electric fields required for the evaporation of aluminium oxide, or poor mechanical stability of the Ni/dielectric/barrier interfaces. These in turn led us to analyze the unprocessed epilayer structures using TEM and APT.

B. Nanoscale structure and chemistry of epitaxy before and after F-implantation and annealing

Figures 3a and c show STEM images from an as-grown wafer imaged along the *a*-zone <11-20> axis, while Figures 3b and d are from an F-implanted wafer along the *m*-zone <1-100> axis. Figures 3a and b present a relative large field view of the layer structure, whereas Figures 3c and d, at higher magnification, reveal the atomic lattices. The thicknesses of the GaN cap and the InAlN/GaN layers are measured as 1.4 ± 0.3 nm and 10.6 ± 0.2 nm respectively in the as-grown sample, and the AlN layer appears as a thin grey band between InAlN and GaN channel, ~ 2-3 atomic (GaN) layers in thickness. These measurements agree well with the epitaxy design.

By comparing Figures 3a and c with Figures 3b and d, it is clear that the GaN cap layer has been removed during plasma F-implantation and the InAlN layer thickness has been reduced significantly. The measured thickness of

the crystalline InAlN/AlN layer is 5.0 ± 0.4 nm, similar to what was observed in the above analysis on the device structures (Figures 1 and 2). This confirms that the reduction in thickness of the crystalline InAlN barrier layer occurs during F-treatment and is not due to over etching of the gate window. As previously mentioned, using AFM, Hu *et al*. also identified an etching effect caused by F-plasma treatment on an InAlN-based structure without a GaN cap,[22] although CF_4 gas was used in that case, rather than the CHF_3 used here. Figure 3d shows that the crystalline region of the barrier material has a rough surface, above which some amorphous material can be seen. Unlike in the device structures, the amorphous material here cannot be AlO_x deposited during the device processing. Hence, this amorphous layer seems likely to be the result of F-implantation induced damage to the barrier layers, which suggests that some of the amorphous material seen immediately above the crystalline barrier material in Figure 1e is damaged InAlN. However, this amorphous material, as well as the topmost crystalline InAlN layers, are very sensitive to high-energy electron beam exposure, so further compositional analysis by STEM-EELS (electron energy loss spectrometry) was not successful. The fragility of these layers may be a result of the damage inflicted by the implantation process.

APT analysis of the unprocessed epilayers is presented in Figure 4, including as-grown and F-implanted samples. It should be mentioned that although APT has been increasingly employed to study semiconductor materials, there are intense debates with regard to fundamental mechanisms and issues in relation to chemical composition quantification.[32,40,41] It has been found that the laser energy has a significant effect on the detection of light elements in nitrides[37,42] and oxides[43]. Therefore in this work, providing consistency with our earlier studies,[30] the compositions reported in Figures 4b and d are expressed as the metallic site fraction, i.e. the quotient of the number of detected atoms of a particular Group III metal element and the total number of detected Group III metal atoms.

Figure 4a is a 3D reconstruction of the APT data arising from the uppermost layers of the as-grown wafer. The figure shows only 10% reconstructed Al atoms (light blue) and 10% reconstructed Ga atoms (yellow) for clarity. The interface relative to GaN channel is highlighted by a 3 site% Al isosurface (the same isosurface composition will also be used in later analyses unless otherwise stated). The corresponding composition profiles calculated using a proximity histogram (proxigram) associated with the isosurface at 3 site % Al are depicted in Figure 4b. The GaN cap layer is observed from these two figures, however, the AlN layer, as identified in Figure 4c, was not distinguished due to its low thickness and aberration of ion trajectories in APT.[32,40] The AlN layer is also likely to contain a significant fraction of Ga atoms.[44]

These data suggest that a large amount of Ga was incorporated into the AlInN layer during MOVPE growth. It is found that Ga was incorporated throughout the entire nominally InAlN layer. Referring now to this layer as a quaternary $In_xAl_{1-x-y}Ga_yN$ layer, the average Ga fraction, y, is 0.23. The In fraction, x, is 0.12, less than the designed In composition level for $In_{0.17}Al_{0.83}N$. However, the In/Al ratio is 0.19, much closer to the designed value of ~ 0.20 in $In_{0.17}Al_{0.83}N$. Assuming that Vegard's law holds for the quanternary alloy, the observed structure would result in about a -0.2 % lattice mismatch with GaN. Within the errors of the compositional analysis, the grown barriers are thus essentially lattice matched with GaN despite not consisting of the ternary AlInN.

A 3D reconstructed image from the F-implanted wafer is illustrated in Figure 4c showing 10% and 50% Ga and oxygen atoms respectively. Since the STEM measurement indicated that the InAlN/AlN thickness of the F-implanted wafer was (5.0 ± 0.4 nm), the APT reconstruction in this case was carried out with the assumption of a 5 nm thick InAlN/AlN layer for simplicity. The resulting compositional profiles are depicted in Figures 4d. As can be seen, a slightly lower In fraction (x = 0.09) than seen for the non-implanted wafer was measured with an In/Al ratio of 0.13 in this case. The F-treated wafer sample was examined using LEAP 3000X HR at laser energy 109 pJ per pulse, which has a nominal detection efficiency of 0.37, whereas the LEAP 5000XR with a nominal

detection efficiency of 0.52 at 0.050 pJ was applied to the as-grown wafer sample. These different analysis conditions may lead to the discrepancy on the observed In/Al ratios. In general, a large detection efficiency favours the detection of multiple-hit events[45,46] and leads to a mass spectrum with increased counts for a given analysed volume, and is thus likely to achieve a more accurate compositional measurement. Although it has been shown that the ratios of metallic sites in InGaN and InAlN layers are relatively stable to moderate changes in the APT analysis conditions,[30,47] a dependency of measured compositions on the surface electric field of emitters has been observed in the analysis of AlGaN layers[48]. In this work, the electric field strength was estimated using the counts ratio of $Al^{2+}/(Al^{+} + Al^{2+} + Al^{3+})$, since the different charge states of ions of same species may reflect the strengths of electric fields around the emitters[49]. Using the Kingham curve,[50] the electric field was estimated to be 22.4 ± 0.3 V nm^{-1} for the case of the as-grown wafer sample and 21.8 ± 0.3 V nm^{-1} for that of the F-treated sample, showing only a marginal difference. Furthermore, the existence of oxygen in the barrier layer would inevitably influence regular evaporation of In-Al-Ga-N-O layers, and subsequently impact the accuracy of composition measurements. The observed slight reductiom in the In/Al ratio in the implanted sample may thus be an artefact of the APT analysis[42], although we cannot rule out the possibility that it is an effect of the F-implantation process.

Considering the difficulties in APT quantification of the light element content as discussed above, the measured oxygen distribution is presented as the count ratio of oxygen over all atoms in Figure 4e. Although a large degree of scattering on the data can be seen in the first ~ 3 nm, the existence of oxygen in the barrier is consistent with the STEM-EDS analysis. The oxygen content can be very crudely estimated by taking into account all detected metallic atoms and oxygen atoms with the assumption that the number of nitrogen atoms is equal to the total number of detected metallic atoms. It should be pointed out that due to the aforementioned problems with light element detection, a Ga/N ratio of 1.6 was measured in the GaN buffer layer in this work. A rough estimate of 15 at. % has been made from APT analysis. This value is much larger than that the STEM-EDS analysis (6 at.%). Despite the large errors in both the STEM-EDS and the APT analysis, the calculated oxygen contents from both techniques, irrespective of the exact value, indicate a high oxygen level present in the barrier after F-implantation, which is significantly above the typical level of a dopant species.

In general, the metallic composition of In, Al and Ga measured by APT from the unprocessed epilayers are consistent with the STEM-EDS analysis on the device. The Ga signal seen in the InAlN barrier layer has been observed on other wafers grown at Cambridge and by other research groups using the same technique in reference [37] and references therein. Its origin may be attributed to the residual Ga-containing materials deposited in the growth environment such as wafer subsector and inner surfaces of precursor delivering pipes.[51] The influence of the unintentionally incorporated Ga and oxygen is discussed with respect to the 2DEG and threshold voltage (see below).

Since plasma-implanted F in the InAlN layer was not detected by APT, a depth profile of F across the InAlN layer was studied on the F-implanted and annealed wafer sample using high depth resolution SIMS.[52] As shown in Figure 4f, the F distribution through the InAlN layer shows an increased concentration at the layer surface which is likely to be a surface artefact. However, a clear shoulder is seen on the surface tail at a depth of about 2 nm. By extrapolating the near surface tail a F concentration of 1.6×10^{19} cm^{-3} can be crudely estimated across the InAlN layer.The SIMS fluorine detection limit is at a level of ~ 2×10^{18} cm^{-3}, equivalent to about 0.002 at.% by a crude estimation, suggesting that the real F-signal is only observed at depth of up to about 5 nm into the barrier layer. Thus, the absence of F in the APT data is likely due to low signal to noise, where the accumulated F counts is indistinguishable from the background of the mass spectrum. The F concentration profile with depth resembles previous analyses on AlGaN-based (RF 150 W)[24] and InAlN-based (RF 150W) E-mode HFETs[28].

C. Evaluation of observed unintentionally incorporated Ga and etched barrier on 2DEG density and threshold voltage

Structural and chemical analysis at nanometer scales revealed that the fabricated device has a quaternary InAlGaN barrier and a reduced barrier thickness below the gate. The effects of these structural changes on device performance, in terms of 2DEG density and threshold voltage have been evaluated using simplified analytical models, in which only spontaneous polarisation was taken into account since, as shown above the unintentional quaternary AlInGaN barrier is approximately lattice-matched to GaN. The compositions used in this analysis are derived from the APT measurements of the unprocessed epilayers. Two type of gate barrier models were used, namely, the nominal $In_{0.17}Al_{0.83}N$ barrier and an $In_{0.10}Al_{0.65}Ga_{0.25}N$ barrier, where the latter is close to the measured barrier composition.

Figure 5a shows the calculated 2DEG density of the two types of barriers as a function of barrier thickness using the following equation:[14]

$$n_s \approx \left[\frac{\sigma_{pol(HFET)}}{q} - \frac{(\phi_B - \Delta E_C)\varepsilon_B}{q d_B} \right] \qquad \text{(Eq.1)}$$

Where $\sigma_{pol(HFET)}$ represents the polarisation charge, q is the charge on an electron, ϕ_B is the metal-semiconductor barrier height, ΔE_C is the conduction band discontinuity, ε_B is the permittivity of barrier and d_B is the thickness of the barrier layer. A 2DEG density of 1.4×10^{13} cm^{-2} is calculated for $In_{0.10}Al_{0.65}Ga_{0.25}N$/GaN with a 10 nm barrier, whereas 2.3×10^{13} cm^{-2} is found for $In_{0.17}Al_{0.83}N$/GaN with the same thickness barrier. The calculated value for the quaternary barrier is consistent with the 2DEG density measured from Hall measurement (1.3×10^{13} cm^{-2}) on the as-grown structure. In general, unintended Ga incorporation is found to lead to a reduced 2DEG density compared with the designed ternary structure at the same barrier thickness. This is predominately due to the reduced bandgap and polarization in InAlGaN over InAlN. It is noted that the 2DEG density of $In_{0.10}Al_{0.65}Ga_{0.25}N$/GaN with a 5 nm barrier as measured in the implanted devices is calculated to be 0.79×10^{13} cm^{-2} and thus the presence of negative charge induced by F-treatment in the barrier is still required to achieve an enhancement mode operation.

Considering negative charges within the barrier, the voltage threshold (V_{th}) of $In_{0.17}Al_{0.83}N$/GaN and $In_{0.10}Al_{0.65}Ga_{0.25}N$/GaN HFETs can be expressed as:

$$V_{th\,(HFET)} = \frac{\phi_B}{q} - \frac{\Delta E_C}{q} - q\frac{d_B}{\varepsilon_B}(\sigma_{pol(HFET)} - Q) - \frac{E_F}{q} \qquad \text{(Eq. 2)}$$

where Q is negative sheet charge in the barrier, E_F is the difference between Fermi level and the conduction band edge of the channel (GaN) (assuming 0.2 eV for all cases), and the rest of ϕ_B, q, ΔE_C, d_B, ε_B and $\sigma_{pol(HFET)}$ are the same as in Eq. 1.

Figure 5b shows the calculated V_{th} of $In_{0.17}Al_{0.83}N$/GaN and $In_{0.10}Al_{0.65}Ga_{0.25}N$/GaN HFETs as a function of barrier thickness. According to the STEM analysis, the barrier has a thickness of ~ 5 nm in the fabricated device (Figure 1). For this given barrier, a negative sheet charge of ~1.35×10^{13}cm^{-2} in the $Al_{0.65}In_{0.10}Ga_{0.25}N$ barrier is required to achieve V_{th} of + 0.8 V based on the Eq. 2. A large positive V_{th} of + 3 V was achieved in F-implanted InAlGaN-based structure with a 20 nm Al_2O_3 gate dielectric layer. The evaluation of V_{th} as a function of barrier

thickness and gate dielectric thickness (neglecting the effect of gate dielectric bulk traps) has been made using the analytical model[27]:

$$V_{th} \approx \frac{1}{q}\left(\phi_{ox} - \Delta E_{ox} - \Delta E_c - E_F\right) - q\frac{d_{ox}}{\varepsilon_{ox}}\left(N_{it} - \sigma_{pol(GaN)} - Q\right) - q\frac{d_B}{\varepsilon_B}\left(\sigma_{pol(HFET)} - Q\right) \qquad \text{(Eq. 3)}$$

Where ϕ_{ox} is the barrier height between Ni metal - Al_2O_3 dielectric (3.5 eV applied[53,54]), ΔE_{ox} conduction band discontinuity between barrier and gate dielectric (assuming 2.1 eV for InAlGaN/Al_2O_3), d_{ox} is the thickness of the dielectric layer, ε_{ox} is the permittivity of gate dielectric, N_{it} is interface trap charge at barrier/oxide interface and $\sigma_{pol(GaN)}$ is polarisation charge density in GaN. Symbol q, ΔE_C, E_F, Q, $\sigma_{pol(HFET)}$, ε_B and d_B are as defined in Eqs. 1 and 2. Using Eq. 3, the negative sheet charge in the barrier and interfacial charge between Al_2O_3/barrier are calculated to be 1.35×10^{13} cm^{-2} and 1.3×10^{13} cm^{-2}, respectively, in order to achieve V_{th} of + 2.8 V in the InAlGaN/GaN structure with a 20 nm Al_2O_3 gate dielectric. The calculated Al_2O_3/barrier interfacial charge is comparable to the reported values for Al_2O_3/AlGaN and Al_2O_3/AlInN.[55,56] With the assumption that there is the same level of F concentration in the wafer structure and device, i.e., an averaged 1.6×10^{19} cm^{-3} across the entire layer, the incorporated F atoms in the InAlN barrier in the device may amount to 9×10^{12} cm^{-2} by taking into account of measured gate width of device (Figure 1). This value is comparable with negative sheet charge estimated using Eq.3.

According to the analytical model, the quaternary nature of the barrier layer may result in an increased V_{th} over that expected for a ternary AlInN layer. This apparent impact arises from the term of $\sigma_{pol(HFET)}$, which has an inverse effect on 2DEG density. These two models imply that the resultant quaternary system may lead to an increased V_{th} but a reduced 2DEG density on the devices. It should be pointed out here that we have not been able to properly model the oxygen rich region at the surface of the barrier in the implanted samples. Since the measured device performance, namely the 2DEG and V_{th} can be essentially explained according to the simplified models without taking into account the observed oxygen in the barrier, which implies that the influence of oxygen should not be large. One might hypothesise that incorporating oxygen at the surface of the barrier would have an effect similar to slightly decreasing the barrier thickness but increasing the dielectric layer. That is, it could marginally reduce the 2DEG density but increase V_{th} according to Eqs. 1 and 3.

IV. CONCLUSION

In summary, we have fabricated E-mode HFETs (V_{th} = + 2.8 V) using a F-treatment process and have investigated the gate region at the nanometer and atomic scale structure using aberration-corrected TEM and APT. This characterisation allowed the identification of unintentional incorporation of Ga across the barrier layer during MOVPE growth resulting in the formation of an InAlGaN quaternary alloy barrier, with a Ga fraction of 0.25. F-based plasma treatment resulted in a reduced barrier thickness, which was observed in the characterisation of both F-treated epilayers and fabricated devices, demonstrating that this is due to the implantation process and not the SiN gate recess etch. In addition to the implantation of F which was characterised by SIMS, we also see evidence for the incorporation of atomic % levels of oxygen into the barrier layers. Based on this information we were then able to study the influence of these deviations from the designed structure on the 2DEG density and V_{th} of the device using simplified analytical models. These models reproduce well the device results and indicate that the resultant InAlGaN device has a reduced 2DEG density but an improved V_{th} over an InAlN structure at a given barrier thickness. Interestingly, despite the noticeable oxygen that is incorporated into the barrier layer during F-implantation, our theoretical calculations suggest that this has little impact on the device. This study shows that in order to fully understand the performance of such E-mode

HFETs, detailed characterisation of the unintended deviations from the device design that occur in the barrier layer during device growth and processing is necessary.

ACKNOWLEDGMENTS

We gratefully acknowledge the financial support from European Research Council under the European Community's Seventh Framework Programme (FP7/2007-2013)/ERC grant agreement no 279361 (MACONS) and Engineering and Physics Science Research Council (EPSRC) under Silicon Compatible GaN Power Electronics (EP/K014471/1). DJ Wallis acknowledges the support of EPSRC through an EPSRC Manufacturing Fellowship in Gallium Nitride EP/N01202X/1.

[1] O. Ambacher, Journal of Physics D: Applied Physics **31,** 2653 (1998).
[2] C. J. Humphreys, MRS bulletin **33,** 459 (2008).
[3] G. Meneghesso, M. Meneghini, I. Rossetto, D. Bisi, S. Stoffels, M. Van Hove, S. Decoutere, and E. Zanoni, Semiconductor Science and Technology **31,** 093004 (2016).
[4] U. K. Mishra, L. Shen, T. E. Kazior, and Y.-F. Wu, Proceedings of the IEEE **96,** 287 (2008).
[5] S. Pearton, B. Kang, S. Kim, F. Ren, B. Gila, C. Abernathy, J. Lin, and S. Chu, Journal of Physics: Condensed Matter **16,** R961 (2004).
[6] M.-S. Lee, D. Kim, S. Eom, H.-Y. Cha, and K.-S. Seo, IEEE Electron Device Letters **35,** 995 (2014).
[7] G. Cywiński, K. Szkudlarek, I. Yahniuk, S. Yatsunenko, M. Siekacz, C. Skierbiszewski, W. Knap, D. B. But, D. Coquillat, and N. Dyakonova, in *GaN/AlGaN based transistors for terahertz emitters and detectors*, 2016 (IEEE), p. 1.
[8] E. Zanoni, M. Meneghini, A. Chini, D. Marcon, and G. Meneghesso, IEEE Transactions on Electron Devices **60,** 3119 (2013).
[9] Y.-F. Wu, D. Kapolnek, J. P. Ibbetson, P. Parikh, B. P. Keller, and U. K. Mishra, IEEE Transactions on Electron Devices **48,** 586 (2001).
[10] A. Crespo, M. Bellot, K. Chabak, J. Gillespie, G. Jessen, V. Miller, M. Trejo, G. Via, D. Walker, and B. Winningham, IEEE Electron Device Letters **31,** 2 (2010).
[11] Z. Zaidi, K. Lee, I. Guiney, H. Qian, S. Jiang, D. Wallis, C. Humphreys, and P. Houston, Semiconductor Science and Technology **30,** 105007 (2015).
[12] G. H. Jessen, R. C. Fitch, J. K. Gillespie, G. Via, A. Crespo, D. Langley, D. J. Denninghoff, M. Trejo, and E. R. Heller, IEEE Transactions on Electron Devices **54,** 2589 (2007).
[13] D. Guerra, R. Akis, F. A. Marino, D. K. Ferry, S. M. Goodnick, and M. Saraniti, IEEE Electron Device Letters **31,** 1217 (2010).
[14] M. Gonschorek, J.-F. Carlin, E. Feltin, M. Py, N. Grandjean, V. Darakchieva, B. Monemar, M. Lorenz, and G. Ramm, Journal of Applied Physics **103,** 093714 (2008).
[15] Y. Cai, Y. Zhou, K. M. Lau, and K. J. Chen, IEEE transactions on electron devices **53,** 2207 (2006).
[16] Y. Uemoto, M. Hikita, H. Ueno, H. Matsuo, H. Ishida, M. Yanagihara, T. Ueda, T. Tanaka, and D. Ueda, IEEE Transactions on Electron Devices **54,** 3393 (2007).
[17] X. Hu, G. Simin, J. Yang, M. A. Khan, R. Gaska, and M. Shur, Electronics Letters **36,** 753 (2000).
[18] W. Lanford, T. Tanaka, Y. Otoki, and I. Adesida, Electronics Letters **41,** 449 (2005).
[19] L.-C. Chang, T.-H. Tsai, Y.-H. Jiang, and C.-H. Wu, in *Enhancement-mode AlGaN/GaN MOS-HEMT on silicon with ultrathin barrier and diluted KOH passivation*, 2016 (IEEE), p. 422.
[20] R. Wang, P. Saunier, Y. Tang, T. Fang, X. Gao, S. Guo, G. Snider, P. Fay, D. Jena, and H. Xing, IEEE Electron Device Letters **32,** 309 (2011).
[21] K. B. Lee, I. Guiney, S. Jiang, Z. H. Zaidi, H. Qian, D. J. Wallis, M. J. Uren, M. Kuball, C. J. Humphreys, and P. A. Houston, Applied Physics Express **8,** 036502 (2015).

[22] Z. Hu, Y. Yue, M. Zhu, B. Song, S. Ganguly, J. Bergman, D. Jena, and H. G. Xing, Applied Physics Express **7,** 031002 (2014).
[23] F. Medjdoub, M. Alomari, J.-F. Carlin, M. Gonschorek, E. Feltin, M. Py, N. Grandjean, and E. Kohn, IEEE Electron device letters **29,** 422 (2008).
[24] Y. Cai, Y. Zhou, K. J. Chen, and K. M. Lau, IEEE Electron Device Letters **26,** 435 (2005).
[25] F. Medjdoub, M. Alomari, J.-F. Carlin, M. Gonschorek, E. Feltin, M. Py, C. Gaquiere, N. Grandjean, and E. Kohn, Electronics Letters **44,** 696 (2008).
[26] R. Wang, Y. Cai, C.-W. Tang, K. M. Lau, and K. J. Chen, IEEE electron device letters **27,** 793 (2006).
[27] Y. Zhang, M. Sun, S. J. Joglekar, T. Fujishima, and T. Palacios, Applied Physics Letters **103,** 033524 (2013).
[28] S. Zhao, J. Xue, P. Zhang, B. Hou, J. Luo, X. Fan, J. Zhang, X. Ma, and Y. Hao, Applied Physics Express **7,** 071002 (2014).
[29] T. Schulz, T. Remmele, T. Markurt, M. Korytov, and M. Albrecht, Journal of Applied Physics **112,** 033106 (2012).
[30] F. Tang, T. Zhu, F. Oehler, W. Y. Fu, J. T. Griffiths, F. C.-P. Massabuau, M. J. Kappers, T. L. Martin, P. A. Bagot, and M. P. Moody, Applied Physics Letters **106,** 072104 (2015).
[31] T. F. Kelly, D. J. Larson, K. Thompson, R. L. Alvis, J. H. Bunton, J. D. Olson, and B. P. Gorman, Annu. Rev. Mater. Res. **37,** 681 (2007).
[32] L. Rigutti, I. Blum, D. Shinde, D. Hernández-Maldonado, W. Lefebvre, J. Houard, F. o. Vurpillot, A. Vella, M. Tchernycheva, and C. Durand, Nano letters **14,** 107 (2013).
[33] B. Mazumder, S. W. Kaun, J. Lu, S. Keller, U. K. Mishra, and J. S. Speck, Applied Physics Letters **102,** 111603 (2013).
[34] J. Roberts, P. Chalker, K. Lee, P. Houston, S. Cho, I. Thayne, I. Guiney, D. Wallis, and C. Humphreys, Applied Physics Letters **108,** 072901 (2016).
[35] http://hyperspy.org/.
[36] P. Geladi, H. Isaksson, L. Lindqvist, S. Wold, and K. Esbensen, Chemometrics and Intelligent Laboratory Systems **5,** 209 (1989).
[37] F. Tang, M. P. Moody, T. L. Martin, P. A. Bagot, M. J. Kappers, and R. A. Oliver, Microscopy and Microanalysis **21,** 544 (2015).
[38] F. Tang, D. Gianola, M. Moody, K. Hemker, and J. Cairney, Acta Materialia **60,** 1038 (2012).
[39] T. Nakao, Y. Ohno, S. Kishimoto, K. Maezawa, and T. Mizutani, physica status solidi (c)**,** 2335 (2003).
[40] T. F. Kelly, A. Vella, J. H. Bunton, J. Houard, E. P. Silaeva, J. Bogdanowicz, and W. Vandervorst, Current Opinion in Solid State and Materials Science **18,** 81 (2014).
[41] H. Tamura, M. Tsukada, K. McKenna, A. Shluger, T. Ohkubo, and K. Hono, Physical Review B **86,** 195430 (2012).
[42] S. Magalhães, N. Franco, I. Watson, R. Martin, K. O'Donnell, H. Schenk, F. Tang, T. Sadler, M. Kappers, R. Oliver, T. Monteiro, T. Martin, P. Bagot, M. Moody, E. Alves, and K. Lorenz, Journal of Physics D: Applied Physics **50,** 205107 (11pp) (2017).
[43] Y. Chen, T. Ohkubo, and K. Hono, Ultramicroscopy **111,** 562 (2011).
[44] D. Wallis, R. Balmer, A. M. Keir, and T. Martin, Applied Physics Letters **87,** 042101 (2005).
[45] D. J. Larson, T. J. Prosa, R. M. Ulfig, B. P. Geiser, and T. F. Kelly, New York, US: Springer Science (2013).
[46] B. Gault, M. P. Moody, J. M. Cairney, and S. P. Ringer, *Atom probe microscopy*, Vol. 160 (Springer Science & Business Media, 2012).
[47] L. Mancini, N. Amirifar, D. Shinde, I. Blum, M. Gilbert, A. Vella, F. Vurpillot, W. Lefebvre, R. Lardé, and E. Talbot, The Journal of Physical Chemistry C **118,** 24136 (2014).
[48] L. Rigutti, L. Mancini, D. Hernandez-Maldonado, W. Lefebvre, E. Giraud, R. Butté, J. Carlin, N. Grandjean, D. Blavette, and F. Vurpillot, Journal of Applied Physics **119,** 105704 (2016).
[49] F. Tang, B. Gault, S. P. Ringer, and J. M. Cairney, Ultramicroscopy **110,** 836 (2010).
[50] D. R. Kingham, Surface Science **116,** 273 (1982).
[51] J. Kim, Z. Lochner, M.-H. Ji, S. Choi, H. J. Kim, J. S. Kim, R. D. Dupuis, A. M. Fischer, R. Juday, and Y. Huang, Journal of Crystal Growth **388,** 143 (2014).

[52] G. Parish, S. Keller, S. Denbaars, and U. Mishra, Journal of Electronic Materials **29,** 15 (2000).
[53] M. Ťapajna and J. Kuzmík, Applied Physics Letters **100,** 113509 (2012).
[54] V. Afanas' ev, M. Houssa, A. Stesmans, and M. Heyns, Journal of applied physics **91,** 3079 (2002).
[55] G. Dutta, S. Turuvekere, N. Karumuri, N. DasGupta, and A. DasGupta, IEEE Electron Device Letters **35,** 1085 (2014).
[56] C. Mizue, Y. Hori, M. Miczek, and T. Hashizume, Japanese Journal of Applied Physics **50,** 021001 (2011).

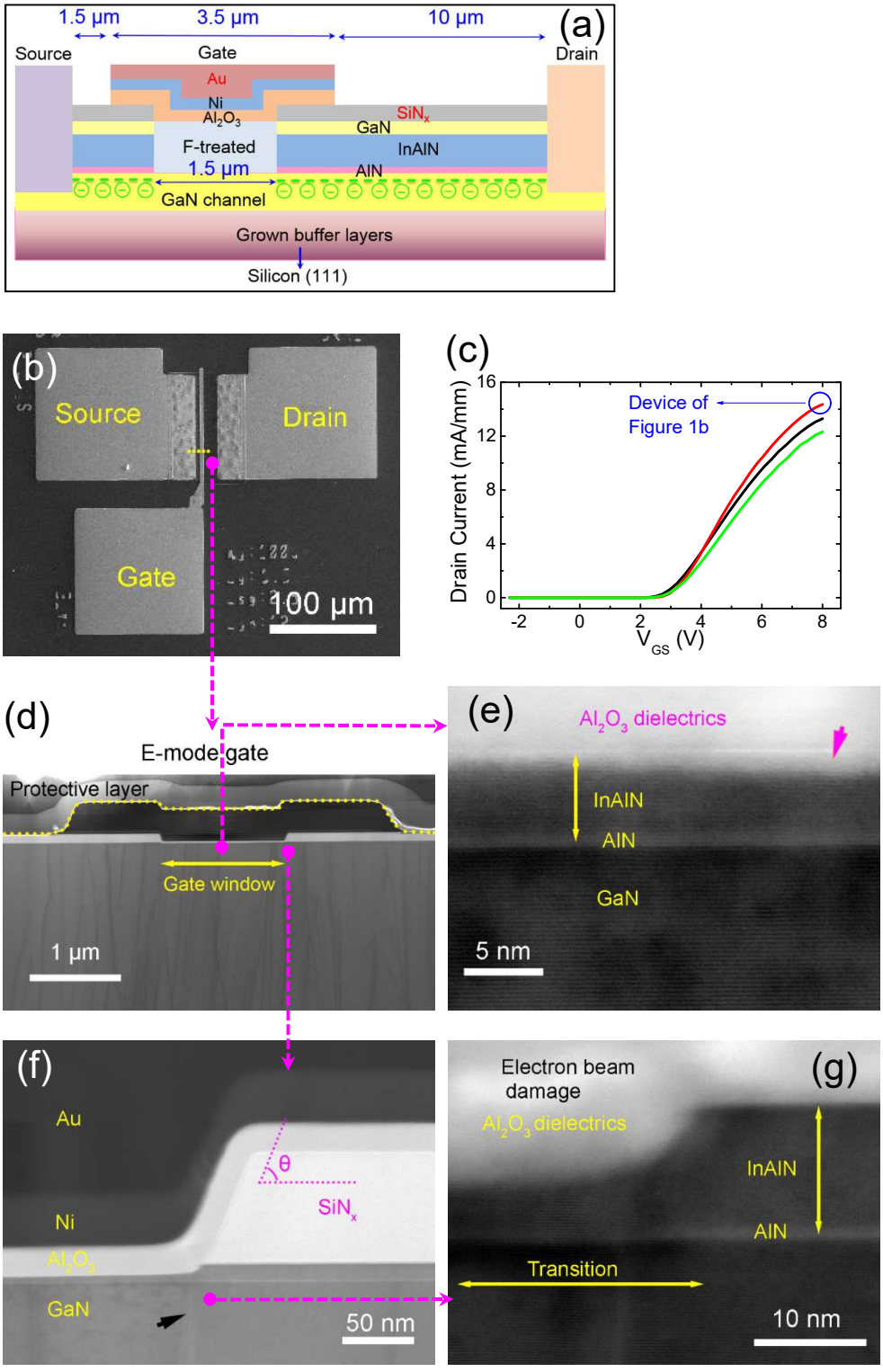

FIG. 1. (a) Schematic illustration (not to scale) of cross-sectional designed MISHFET device grown on a Si (111) wafer; (b) a fabricated MISHFET transistor, where the dotted line indicating the position for the cross-sectional STEM-BF analysis of gate areas (*m*-zone axis) in (d) - (g); (c) gate transfer characteristics of device I_d vs V_{gs} (three devices), where the one circled is from the corresponding device in (b); (d) an entire view of gate; (e) high resolution image of InAlN layer at the gate central areas; (f) the right gate edge indicating layered structures Al, Ni, Al_2O_3, InAlN and GaN layers, as well as SiN_x passivation layers and (g) high magnification image of the recessed InAlN layer at the gate edge.

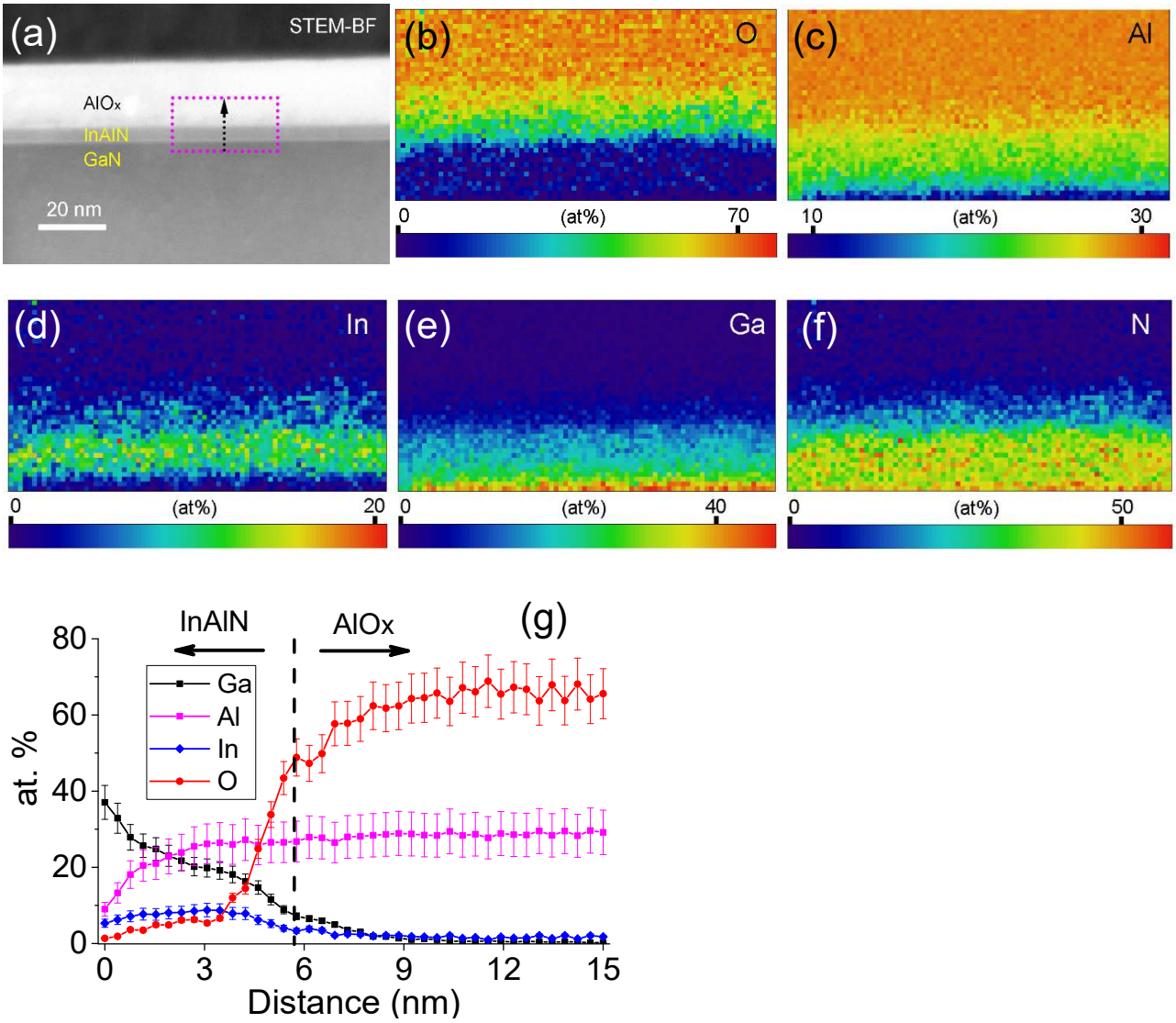

FIG. 2. Elemental mapping of gate area by STEM-EDS. (a) STEM-BF image, where the rectangular area (15.4 × 30.8 nm) is designated the EDS mapping region and the dotted line shows the plotting direction in (g). (b), (c), (d), (e) and (f) are the distributions of O, Al, In, Ga and N elements correspondingly, and (g) are the profiles of Ga, Al, In and O elements extracted from the central mapped region in (a) with a line width of 15 nm.

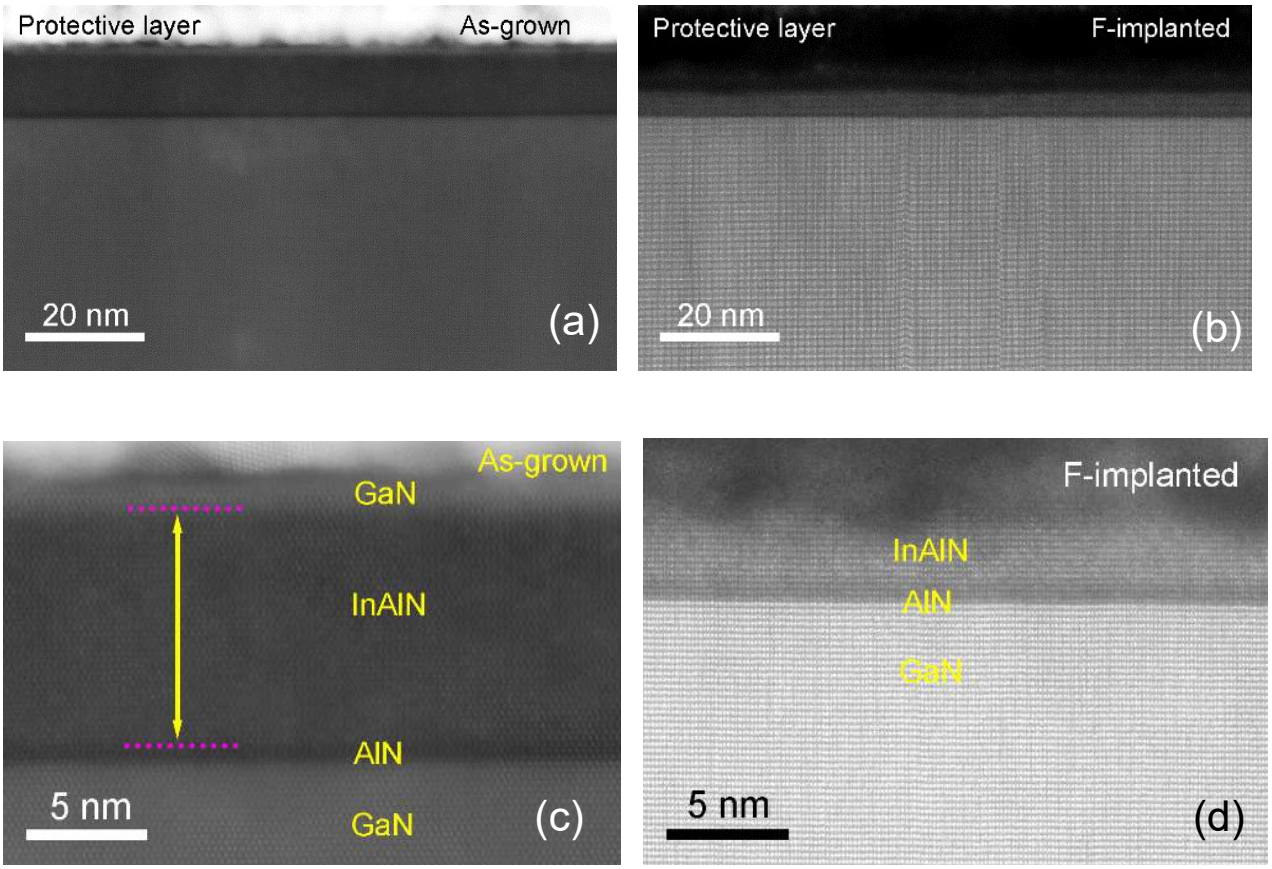

FIG. 3. STEM-HAADF imaging cap-GaN/InAlN/AlN/GaN layers. (a) and (c) as-grown wafer structure (*a*-zone axis). (b) and (d) F-implanted (*m*-zone axis) and annealed wafers, showing the recessed InAlN layers (InAlN/GaN as grown 10.6 nm; F-planted 5.0 nm).

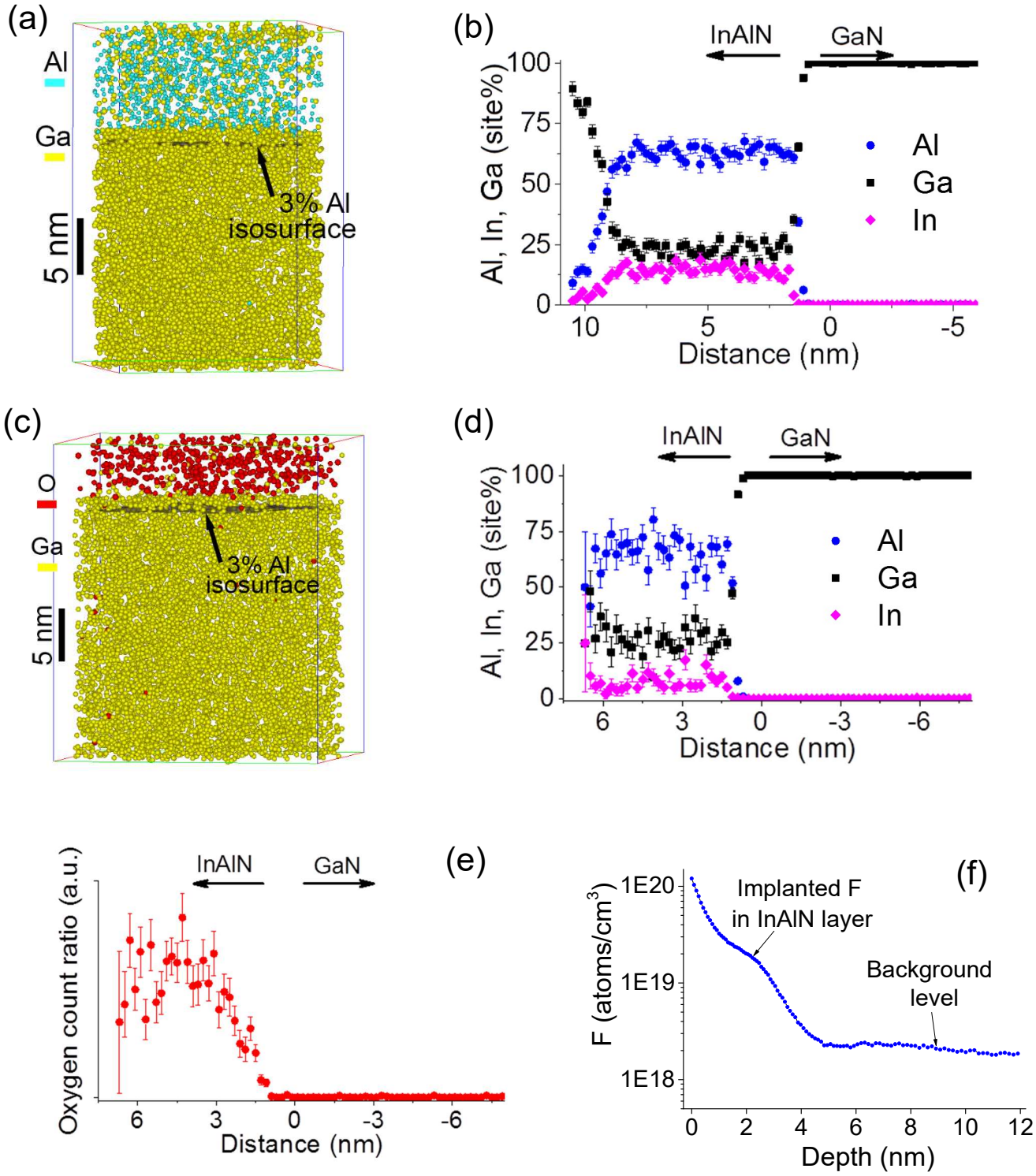

FIG. 4. (a) APT 3D analysis of as-grown wafter showing reconstructed 10% Al atoms and 10% Ga atoms respectively, where the interface of InAlN/GaN is marked by the 3% site Al isosurfaces; (b) the corresponding concentration profiles of Al, In and Ga atoms calculated using proximate histogram (proxigram) through the depth by 3% Al; (c) APT reconstructed 3D image on the F-implanted sample represented by the 50% oxygen atoms and 10% Ga atoms and the interfaces are highlighted by 3% Al isosurface; (d) the proxigram concentration profiles of Al, In and Ga metallic site; (e) the count ratio profile of oxygen over all atoms; and (f) SIMS analysis of F profile implanted in the annealed wafer sample.

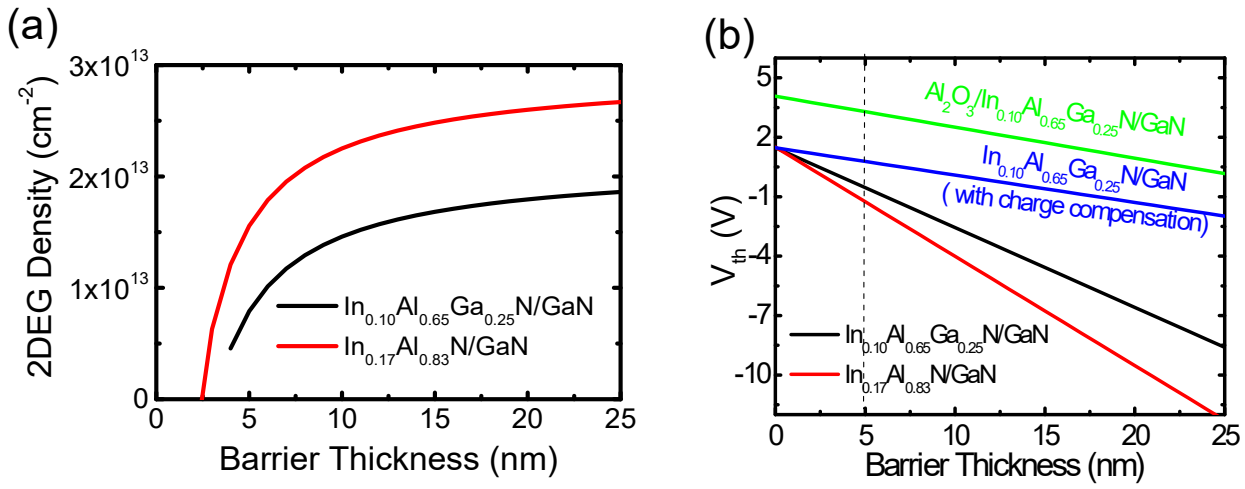

FIG. 5. Calculated 2DEG density (a) and threshold voltage (b) as a function of barrier thickness respectively. The negative sheet charges in the barrier and interfacial charge between Al_2O_3/barrier are calculated to be 1.4 × 10^{13} cm^{-2} and 1.2 ×10^{13} cm^{-2} respectively, in order to achieve V_{th} of + 2.8 V in the InAlGaN/GaN structure at a 20 nm Al_2O_3 gate dielectric. (Spontaneous polarisation was taken into account only in the calculations. Details in text)